Dynamics of Atmospheres and Oceans 71 (2015) 98–107

Contents lists available at ScienceDirect

Dynamics of Atmospheres and Oceans

journal homepage: www.elsevier.com/locate/dynatmoce

On the instability of a buoyancy-driven downflow

Albert Dai *

Department of Engineering Science and Ocean Engineering, National Taiwan University, Taipei, Taiwan

ARTICLE INFO

Article history:
Received 11 September 2014
Received in revised form 30 June 2015
Accepted 30 June 2015
Available online 4 July 2015

Keywords:
Gravity currents
Buoyancy-driven flows
Instability

ABSTRACT

Gravity currents flowing downslope, namely downflows, were observed to have a larger scale instability on high slope angles and such violent instability was absent for downflows on low slope angles. By linear theory, it is found that two branches of instability occur for slope angle in the range of $0^\circ < \theta < 90^\circ$. The ensuing instability is on the upper branch for low slope angles and on the lower branch for high slope angles. There also exists a transitional slope angle, $\theta_E \approx 0.04^\circ$, at which the onset instability switches from one branch to the other. The scale of instability is found to increase and tend to skew towards the upper edge of the downflow as the ensuing instability switches from the upper branch to the lower one. Our findings surprisingly resonate with previously reported observations. Critical Reynolds number, below which the flow is stable to infinitesimal disturbances, is found to increase as the slope angle decreases. The role played by the bottom slope is essentially twofold. On one hand, the downslope component of gravity acts as the driving force for downflows. On the other hand, the wall-normal component of gravity acts for the stratification effect. Therefore, as the slope angle decreases, the driving force diminishes and the stratification intensifies, which can explain that the critical Reynolds number increases as the slope angle decreases. When a downflow propagates onto a sufficiently low slope angle, the low driving force and intensified stratification effect would make the downflow less prone to sustain a turbulent state of flow, which ultimately leads to the final stage of a gravity current event.

1. Introduction

Gravity currents, otherwise known as buoyancy or density currents, are flows of dense fluid beneath light ambient fluid, or light fluid above dense ambient fluid, primarily in the horizontal direction (Huppert, 2006). These flows are gravitationally driven by the density difference between the fluid in the currents and its environment and are quite common in natural and man-made environments (Allen, 1985; Fannelop, 1994; Simpson, 1997). A number of factors can cause variations in the density of fluid, which include temperature differentials, dissolved materials, and suspended sediments. While lock-exchange flows, in which gravity currents are produced from a finite buoyancy source released instantaneously on a horizontal boundary, have drawn much attention in the literature (e.g. Shin et al., 2004; Marino et al., 2005; Cantero et al., 2007; La Rocca et al., 2; Adduce et al., 2012), gravity currents over sloping terrain are also commonly encountered in nature. Prominent examples include dense overflows in the ocean (Nielsen et al., 2004; Dai and Garcia, 2010; Dai, 2010, 2013b) and powder-snow avalanches (Beghin et al., 1981; Hopfinger, 1983; Rastello and Hopfinger, 2004). In the laboratory, gravity currents on a slope can be produced from a sudden release of a finite volume of dense fluid (Maxworthy, 2010; Dai, 2013a) or

* Tel.: +886 2 33665790.
E-mail address: hdai@ntu.edu.tw

http://dx.doi.org/10.1016/j.dynatmoce.2015.06.004
0377-0265/

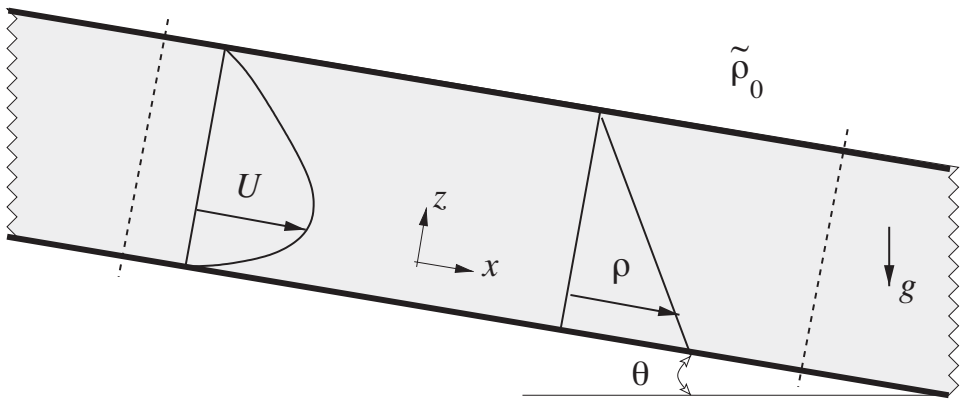

Fig. 1. Sketch of a downflow with a top wall driven by a linear density excess. The bottom slope makes an angle θ with the horizontal direction. The channel is open to the environment at both ends and there is no net pressure gradient acting on the flow. The flow represents an idealised model of a downflow in which entrainment of ambient fluid is not allowed in the channel.

from a steady source of dense fluid into a uniform (Britter and Linden, 1980) or stratified environment (Baines, 2001, 2005). Direct numerical simulations also provide a useful means to study the gravity currents on sloping boundaries (Cantero et al., 2009, 2009; Shringarpure et al., 2012). On a point of terminology, here we use the term 'downflow' to refer to the downslope propagating gravity current produced from a steadily maintained buoyancy inflow.

This paper is motivated by the recent observation reported by Talling et al. (2007) from the analysis of sediment cores that a transition of flow for a turbidity current event in the Agadir basin offshore from northwest Africa, marked by sediment deposition, could be triggered by a small but abrupt decrease of slope from 0.05° to 0.01°. The turbidity current propagated on the 0.05° slope for ∼100 km and continued on the 0.01° slope for a further ∼250 km. Sediment deposition was very little on the 0.05° slope and mainly on the 0.01° slope. This abrupt transition of flow is similar to the onset of hydrodynamic instability, but it was not determined unequivocally whether this flow transition is from one turbulent state to another or a reverse-transition from turbulent to laminar flows. Simple calculations and evidence for fast flow velocities as documented in Talling et al. (2007) indicate that the transition from one turbulent state to another is more likely, albeit without theoretical support.

Aiming at providing a theoretical support for the reported observation, we adopt a heuristic model, namely the 'downflow with a roof' configuration, and perform the stability analysis for the gravity currents down different bottom slopes. The analysis will be carried out based upon a two-dimensional buoyancy-driven base flow, of which the stability properties are of particular interest. Of course in the field the flow is rarely two-dimensional, however, from a theoretical point of view it is sufficient to consider only the two-dimensional problem to find the least stable conditions, i.e. Squire's theorem (Drazin and Reid, 1981). For a more thorough review and references on buoyancy-driven shear flow in a channel, the readers can be referred to Chen and Pearlstein (1989). In particular, it is worth noting that Birikh (1966), Birikh et al. (1968, 1972), Hart (1971) considered the stability of a plane-parallel flow in a channel where the top and bottom walls are heated differently. Such a stability problem is similar in configuration to but is different from the one investigated here. While in Birikh (1966), Birikh et al. (1968, 1972), Hart (1971) the buoyancy, or temperature, is maintained at different levels on the walls, i.e. Dirichlet type boundary conditions, here it is assumed no buoyancy flux across the boundaries, i.e. Neumann type boundary conditions. As will be discussed later, our results indicate two branches of instability which were not observed previously in these references.

The 'downflow with a roof' configuration has been widely employed in the study of buoyancy-driven flows on sloping boundaries, e.g. Cantero et al. (2009), Shringarpure et al. (2012). In this configuration, both ends of the channel are open to the environment and consequently, the flow within the channel is purely driven by the density excess of the downflow fluid. In reality, the downflows generally do not have a distinct upper boundary as shown in Fig. 1, but entrain ambient water across a more diffuse upper boundary. The thickness of the downflow, therefore, tend to slowly increase in the downslope direction due to ambient water entrainment. In the 'downflow with a roof' configuration, the slow development of the current as the downflow propagates is ignored by not allowing entrainment of ambient fluid. Notwithstanding, the 'downflow with a roof' configuration preserves a key element in the downflow problem, i.e. the flow is purely driven by the density excess, and allows for a steady state, uniform solution as a basis for the stability analysis.

To facilitate the analysis, we adopt a linear density excess profile, with a density excess $\Delta\tilde{\rho}_b$ at the bottom and no density excess on the top wall, within the channel for the body of a gravity current. That the density excess diminishes in the wall-normal direction away from the bottom can be a consequence of self-stratification effects in sediment-laden downflows, dilution due to entrained ambient fluid, or diffusion. There has been a large number of experimental works undertaken to analyse the velocity and density structures of a gravity current (McCaffrey et al., 2003; Choux et al., 2005; Felix et al., 2005). Simple as the linear density excess profile can be, it not only preserves the essential feature of the density profile in the body of a gravity current (Choux et al., 2005) but also self-consistently satisfies the equation of buoyancy

conservation as a steady state, uniform solution. It is known that when the density excess is uniform across the channel depth, the problem is equivalent in a mathematical sense to a purely pressure-driven channel flow with no stratification effects (Cantero et al., 2009). To recreate the downflows in the laboratory with a roof and with specified velocity and density profiles is difficult, but the simple mathematical model of downflows employed in this study helps develop understanding of different characteristics of downflows on high and low slope angles.

Our results support the observation that the flow transition was likely from one turbulent state to another and imply that such flow transition could occur in similar deep ocean environment. This paper is organised as follows. The linear stability analysis of the downflow, including the steady state, uniform base flow, is presented in Section 2. The numerical method used to solve the stability eigenvalue problem is presented in Section 3. Results are summarized in Section 4 and finally conclusions are drawn in Section 5.

2. Linear stability analysis

The downflow in this study is modeled as a continuous buoyancy flow with a top wall driven by a linear density excess, as shown in Fig. 1. The inclined bottom forms an angle θ with the horizontal direction. Here the thickness of the flow, namely the distance between the walls or $\tilde{H}$, is chosen as the length scale. The density of fluid in the channel is $\tilde{\rho}$, the density excess at the bottom is $\Delta\tilde{\rho}_b$, and the density of ambient fluid is $\tilde{\rho}_0$. The velocity scale of the problem is therefore chosen as $\tilde{u}_b = \sqrt{\Delta\tilde{\rho}_b g \sin\theta \tilde{H}/\tilde{\rho}_0}$. Here we assume that the density excess is sufficiently small such that the Boussinesq approximation is valid and the dimensionless governing equations take the following form:

$$\nabla \cdot \mathbf{u} = 0, \tag{1}$$

$$\frac{\partial \mathbf{u}}{\partial t} + \mathbf{u}\cdot\nabla\mathbf{u} = -\nabla p + \frac{1}{Re}\nabla^2\mathbf{u} + \rho\mathbf{e}_g, \tag{2}$$

$$\frac{\partial \rho}{\partial t} + \mathbf{u}\cdot\nabla\rho = \frac{1}{ReSc}\nabla^2\rho. \tag{3}$$

where $\mathbf{u} = (u, 0, w)$ is the velocity, $\mathbf{e}_g = (1, 0, -1/\tan\theta)$ is the direction of gravity. Please note that with the velocity scale $\tilde{u}_b$ defined above, the gravity vector is $(1, 0, -1/\tan\theta)$ rather than $(\sin\theta, 0, -\cos\theta)$, where the term $1/\tan\theta$ represents the ratio of the wall-normal component of gravity to the streamwise component of gravity. The dimensionless density excess is defined as

$$\rho = \frac{\tilde{\rho} - \tilde{\rho}_0}{\Delta\tilde{\rho}_b}. \tag{4}$$

The dimensionless parameters arising from the normalisation are

$$Re = \frac{\tilde{u}_b \tilde{H}}{\tilde{\nu}}, \quad Sc = \frac{\tilde{\nu}}{\tilde{\kappa}}. \tag{5}$$

where $\tilde{\nu}$ is the kinematic viscosity and $\tilde{\kappa}$ is the diffusivity of the density field. Typically for turbidity currents, the Schmidt number is greater than unity. However, based on the reports that the influence of Schmidt number is weak as long as it is $O(1)$ or larger (Härtel et al., 2000; Necker et al., 2005; Cantero et al., 2007; Bonometti and Balachandar, 2008), it has become a custom in the computational study of gravity currents to set $Sc = 1$ and we follow suit here and employ $Sc = 1$ in the study.

2.1. Base flow

The downflow is modeled as a buoyancy flow driven by a linear density excess profile, i.e. $\bar{\rho}(z) = 1 - z$. Upon substitution into (2.2) and with no-slip condition at the walls, a steady state velocity profile is derived as

$$U(z) = Re\left(\frac{1}{6}z^3 - \frac{1}{2}z^2 + \frac{1}{3}z\right). \tag{6}$$

Fig. 2 shows (a) the steady state velocity and (b) the shear stress profiles. As we note the maximum velocity occurs at $z \approx 0.423$, which is slightly below the centerline of the channel. The maximum shear stress occurs at $z = 0$ and decreases away from the bottom. The location where shear stress passes through zero, $z \approx 0.423$, also represents the point of inflection in the velocity profile. In a real turbidity current, the location at which the maximum streamwise velocity occurs is close to the bottom and further away from the bottom the streawise velocity decreases more gradually to zero. The velocity profile in Fig. 2 is similar to a real turbidity current in the sense that the location of maximum streamwise velocity is skewed towards the bottom rather than on the centerline of the channel as in a pressure-driven velocity profile.

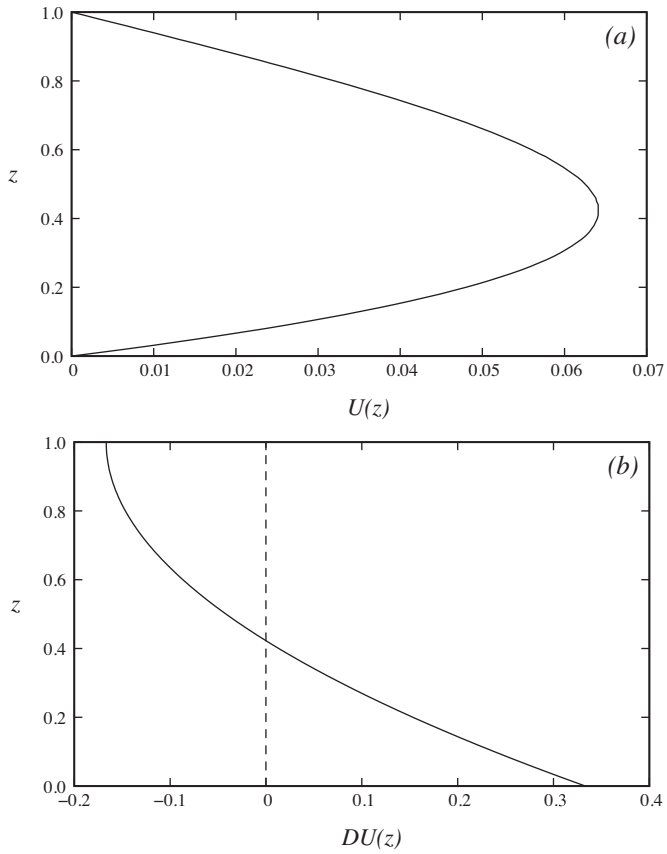

Fig. 2. Steady state velocity profile, plotted in panel (a), and shear stress profile, plotted in panel (b), of the mean flow driven by a linear density excess, $\bar{\rho} = 1 - z$, where D denotes derivative with respect to z. The maximum mean flow velocity occurs at $z \approx 0.423$, which is slightly below the centerline of the channel.

2.2. Disturbance equations

In order to investigate the stability property of flow using (1)–(3), we adopt the linear stability analysis which introduces the velocity, pressure, and density excess in the perturbed form

$$u = U + u', \quad w = w', \quad p = p_0 + p', \quad \rho = \bar{\rho} + \rho'. \tag{7}$$

Upon substitution of (7) into (1)–(3) and linearisation, we have

$$\frac{\partial u'}{\partial x} + \frac{\partial w'}{\partial z} = 0, \tag{8}$$

$$\frac{\partial u'}{\partial t} + U\frac{\partial u'}{\partial x} + w'\frac{dU}{dz} = -\frac{\partial p'}{\partial x} + \rho' + \frac{1}{Re}\left(\frac{\partial^2 u'}{\partial x^2} + \frac{\partial^2 u'}{\partial z^2}\right), \tag{9}$$

$$\frac{\partial w'}{\partial t} + U\frac{\partial w'}{\partial x} = -\frac{\partial p'}{\partial z} - \frac{1}{\tan\theta}\rho' + \frac{1}{Re}\left(\frac{\partial^2 w'}{\partial x^2} + \frac{\partial^2 w'}{\partial z^2}\right), \tag{10}$$

$$\frac{\partial \rho'}{\partial t} + U\frac{\partial \rho'}{\partial x} + w'\frac{d\bar{\rho}}{dz} = \frac{1}{ReSc}\left(\frac{\partial^2 \rho'}{\partial x^2} + \frac{\partial^2 \rho'}{\partial z^2}\right), \tag{11}$$

where $\rho'/\tan\theta$ represents the buoyancy term in the perturbation equations and $1/\tan\theta$ essentially plays the role of the Richardson number, as will be discussed further in Section 5. Here the perturbed velocity can be expressed in terms of the streamfunction ψ' as

$$u' = \frac{\partial \psi'}{\partial z} \quad \textit{and} \quad w' = -\frac{\partial \psi'}{\partial x}, \tag{12}$$

and the disturbances can be expanded in terms of normal modes, i.e.

$$\psi' = \hat{\phi}(z)e^{i(\alpha x-\omega t)}, \quad p' = \hat{p}(z)e^{i(\alpha x-\omega t)}, \quad \rho' = \hat{\rho}(z)e^{i(\alpha x-\omega t)}. \tag{13}$$

Upon substitution of (12) and (13) into (9)–(11) and eliminating the pressure term, a set of sixth order differential equations forms the eigenvalue problem

$$\begin{aligned} i\alpha\left(D^2U\hat{\phi}+\alpha^2U\hat{\phi}-UD^2\hat{\phi}\right) \quad &+ \quad D\hat{\rho}+\frac{i\alpha}{\tan\theta}\hat{\rho}+\frac{1}{Re}\left(D^4\hat{\phi}-2\alpha^2D^2\hat{\phi}+\alpha^4\hat{\phi}\right) \\ &= i\omega\left(\alpha^2\hat{\phi}-D^2\hat{\phi}\right), \end{aligned} \tag{14}$$

$$i\alpha\left(\hat{\phi}+U\hat{\rho}\right)+\frac{1}{ReSc}\left(\alpha^2\hat{\rho}-D^2\hat{\rho}\right)=i\omega\hat{\rho}, \tag{15}$$

where D denotes derivative with respect to z. Here temporal stability problem is pursued where α is the wavenumber in the x direction taken to be real and the eigenvalue $\omega = \omega_r + i\omega_i$ is the frequency assumed to be complex, of which the imaginary part, i.e. ω_i, determines the growth rate of disturbance. In other words, $\omega_i \leq 0$ indicates that the flow is stable to infinitesimal disturbances and otherwise unstable. The eigenvalue problem is completed with no-slip condition at the walls, i.e.

$$\phi = D\phi = 0 \quad at \quad z = 0, 1, \tag{16}$$

and no mass flux across the boundaries, i.e.

$$D\rho = 0 \quad at \quad z = 0, 1. \tag{17}$$

We may solve the eigenvalue problem with matrix method to obtain the eigenvalue ω. Here the no mass flux boundary conditions indicate that there is no buoyancy-exchange across the bottom and top walls. In the literature, the buoyancy-conserving flow in which there is zero net flux of sediments to or from the bed is also said to be in bypass or auto-suspension mode. In this study, essentially we are considering a downflow with a linear density excess profile while there is no buoyancy-exchange between the flow and the boundaries during the propagation. The linear density excess profile is taken as the ansatz in the problem formulation, rather than a self-evident solution derived directly from (3) and (17). It may seem odd to some readers that the linear density excess profile does not satisfy (17). In fact, the straightforward solution for the density excess profile derived from (3) and (17), namely a uniform density excess across the depth, is trivial. As explained by Cantero et al. (2009), the 'downflow with a roof' problem with a uniform density excess is equivalent to a Poiseuille flow and does not serve the purpose in the study.

3. Numerical method

Our intent is to solve the eigenvalue problem numerically. The amplitudes of the disturbances, namely $\hat{\phi}$ and $\hat{\rho}$, are expanded in the following form:

$$\hat{\phi}(z) = \sum_{n=1}^{N} a_n\hat{\phi}_n(z) \quad and \quad \hat{\rho}(z) = \sum_{n=1}^{N} b_n\hat{\rho}_n(z), \tag{18}$$

in which a_n's and b_n's are undetermined coefficients and each basis function, i.e. $\hat{\phi}_n$ and $\hat{\rho}_n$ ($n = 1, 2, \ldots, N$), is individually a linear combination of Chebyshev polynomials of the first kind, T_n. Specifically, the basis functions are defined as

$$\hat{\phi}_n = \sum_{j=0}^{4} c_j T_{n-1+j} \quad \text{and} \quad \hat{\rho}_n = \sum_{j=0}^{2} d_j T_{n-1+j},$$

where c_j's and d_j's are defined such that the four boundary conditions on $\hat{\phi}_n$, i.e. (16), and two boundary conditions on $\hat{\rho}_n$, i.e. (17), are satisfied for each $\hat{\phi}_n$ and $\hat{\rho}_n$, respectively.

We employ Galerkin method to formulate the problem in a matrix form (Chandrasekhar, 1981; Drazin and Reid, 1981). After substituting (18) into (14) and (15) and requiring the weighted residual be zero with respect to $\hat{\phi}_n$ and $\hat{\rho}_n$ ($n = 1, 2, \ldots, N$), we derive a generalized eigenvalue probelm:

$$\mathbf{Ax} = \omega\mathbf{Bx}, \tag{19}$$

where

$$\mathbf{A} = \begin{pmatrix} \mathcal{A}_{11} & \mathcal{A}_{12} \\ \mathcal{A}_{21} & \mathcal{A}_{22} \end{pmatrix} \quad and \quad \mathbf{B} = \begin{pmatrix} \mathcal{B}_{11} & \mathcal{B}_{12} \\ \mathcal{B}_{21} & \mathcal{B}_{22} \end{pmatrix}, \tag{20}$$

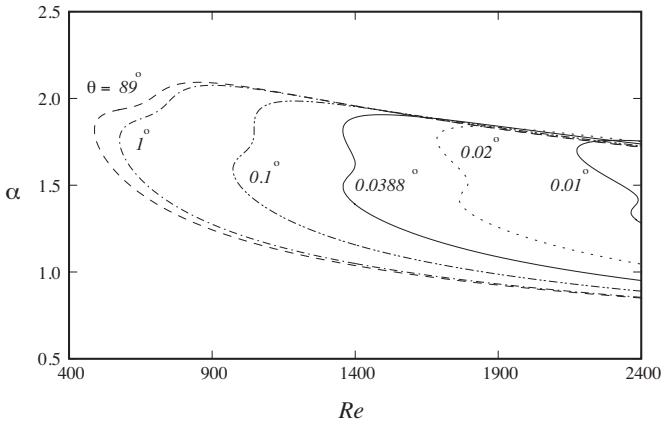

Fig. 3. Neutral stability curve in the (α, Re) plane for the downflow. The slope angles are chosen at $\theta = 0.01^\circ$, 0.02°, 0.0388°, 0.1°, 1°, 89° for illustrative purposes.

and $\mathbf{x} = (a_1, a_2, \ldots, a_N, b_1, b_2, \ldots, b_N)^T$. Here $\mathbf{A}$ and $\mathbf{B}$ are matrices of $2N \times 2N$ and their elements, namely $\mathcal{A}_{11}$, $\mathcal{A}_{12}$, $\mathcal{A}_{21}$, $\mathcal{A}_{22}$, $\mathcal{B}_{11}$, $\mathcal{B}_{12}$, $\mathcal{B}_{21}$, $\mathcal{B}_{22}$, are matrices of $N \times N$ and, in indicial notation, are

$$\begin{aligned}\mathcal{A}_{11ij} &= i\alpha\left(\left\langle\hat{\phi}_i, D^2U\hat{\phi}_j\right\rangle + \alpha^2\left\langle\hat{\phi}_i, U\hat{\phi}_j\right\rangle - \left\langle\hat{\phi}_i, UD^2\hat{\phi}_j\right\rangle\right) + \\ &\quad \frac{1}{Re}\left(\left\langle\hat{\phi}_i, D^4\hat{\phi}_j\right\rangle - 2\alpha^2\left\langle\hat{\phi}_i, D^2\hat{\phi}_j\right\rangle + \alpha^4\left\langle\hat{\phi}_i, \hat{\phi}_j\right\rangle\right),\end{aligned} \tag{21}$$

$$\mathcal{A}_{12ij} = \left\langle\hat{\phi}_i, D\hat{\rho}_j\right\rangle + \frac{i\alpha}{\tan\theta}\left\langle\hat{\phi}_i, \hat{\rho}_j\right\rangle, \tag{22}$$

$$\mathcal{A}_{21ij} = i\alpha\left\langle\hat{\rho}_i, \hat{\phi}_j\right\rangle, \tag{23}$$

$$\mathcal{A}_{22ij} = i\alpha\left\langle\hat{\rho}_i, U\hat{\rho}_j\right\rangle + \frac{1}{ReSc}\left(\alpha^2\left\langle\hat{\rho}_i, \hat{\rho}_j\right\rangle - \left\langle\hat{\rho}_i, D^2\hat{\rho}_j\right\rangle\right), \tag{24}$$

$$\mathcal{B}_{11ij} = i\left(\alpha^2\left\langle\hat{\phi}_i, \hat{\phi}_j\right\rangle - \left\langle\hat{\phi}_i, D^2\hat{\phi}_j\right\rangle\right), \tag{25}$$

$$\mathcal{B}_{22ij} = i\left\langle\hat{\rho}_i, \hat{\rho}_j\right\rangle, \tag{26}$$

where $i, j = 1, 2, \ldots, N$ and $\langle\cdot\rangle$ denotes the weighted inner product in L^2 norm. Here $\mathcal{B}_{12}$ and $\mathcal{B}_{21}$ are zero matrices. The inner products of Chebyshev polynomials are exactly integrated with Gaussian quadrature. The numerical method, namely spectral method, has a very high order of approximation in that the error decreases exponentially as opposed to algebraically for finite-difference methods. The number of basis functions, N, is chosen sufficiently large to exploit spectral convergence (Boyd, 2001). In our study that follows, $N = 80$ is used in the computation after the test on the number of basis functions. The generalized eigenvalue problem is then solved by LAPACK routines.

4. Results

We repeated the computation for (19) over a wide range of α and Re for a number of slope angles and searched for the neutral stability curve, on which the growth rate is zero, i.e. $\omega_i = 0$. Fig. 3 shows the neutral stability curves in the (α, Re) plane for different slope angles. The region inside the neutral curve for each slope angle corresponds to instability while the region outside the curve corresponds to stability. We observe not only one but two branches of eigensolution. Of course, multiple eigensolutions depicting neutral stability curve are not uncommon in this type of analysis, but notable here is that the two branches are usually well separated with distinct onset Reynolds numbers and wavenumbers. It is also observed that there exists a slope angle, $\theta_E = 0.0388^\circ$, at which the onset Reynolds numbers of the two branches are equal, at $Re_E = 1356.66$. For slope angles below θ_E, the onset instability occurs on the upper branch with higher onset wavenumbers, while for slope angles above θ_E, the onset instability occurs on the lower branch with lower onset wavenumbers. As the slope angle increases through θ_E, we see from Fig. 3 that the onset wavenumber switches from about 1.81 to 1.49. Therefore, we would expect the scale of instability to increase as the bottom slope increases from low slope to high slope angles.

Note that for each slope angle, there exists a minimum Reynolds number, namely the critical Reynolds number Re_{crit}, such that for all Reynolds number below this value the flow is stable to infinitesimal disturbances. Fig. 4 shows Re_{crit} versus θ for the downflow. It is observed that for bottom slopes in the range of $10^\circ \lesssim \theta \leq 89^\circ$, the critical Reynolds number is in a relatively narrow range of $480 < Re_{crit} < 500$ but the critical Reynolds number increases rapidly when the bottom slope decreases below 10°, as shown by the inset of Fig. 4. When a downflow propagates on a slope which decreases during the

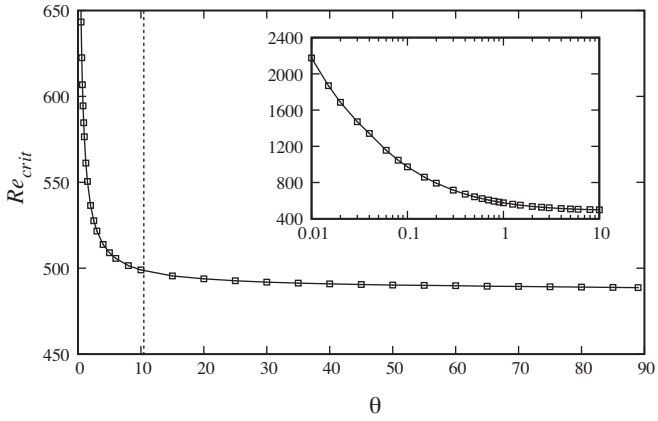

Fig. 4. Critical Reynolds number, Re_{crit}, against slope angle, θ, for $0.01^\circ \le \theta \le 89^\circ$. Inset figure shows close-up view of Re_{crit} versus θ for $0.01^\circ \le \theta \le 10^\circ$.

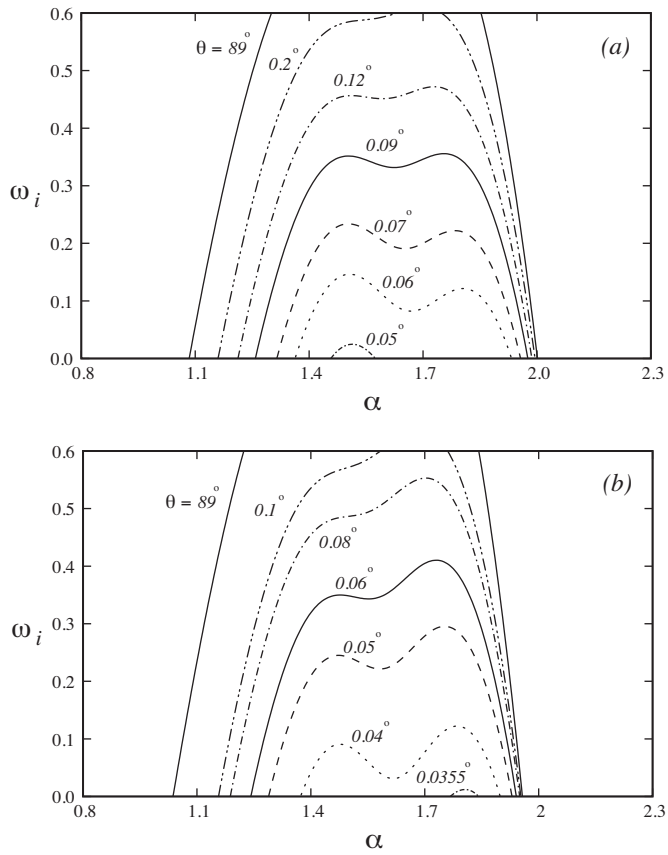

Fig. 5. Growth rate, ω_i, against wavenumber, α, at $Re = 1250$ (a) and $Re = 1400$ (b). For illustrative purposes, slope angles are chosen at $\theta = 0.05^\circ$, 0.06°, 0.07°, 0.09°, 0.12°, 0.2°, 89° in (a) and chosen at $\theta = 0.0355^\circ$, 0.04°, 0.05°, 0.06°, 0.08°, 0.1°, 89° in (b).

course of its motion, as is the case of the continental slope on the ocean floor, the increasing critical Reynolds number makes the downflow less prone to sustain a turbulent state of flow, which inevitably leads to the final stage of a gravity current event.

The existence of the two branches of instability can be alternatively illustrated by the growth rate curve in the (ω_i, α) plane. Holding Reynolds number at $Re = 1250$ and looking at the growth rate, ω_i, as a function of wavenumber, α, for different slope angles, we find from Fig. 5(a) that the onset instability occurs on the lower branch at $\theta = 0.05^\circ$. The growth rates on the lower and upper branches both increase as the slope angle increases, but the growth rate on the lower branch is higher than the upper branch until $\theta \approx 0.09^\circ$. Now when holding Reynolds number at $Re = 1400$, we find from Fig. 5(b) that the

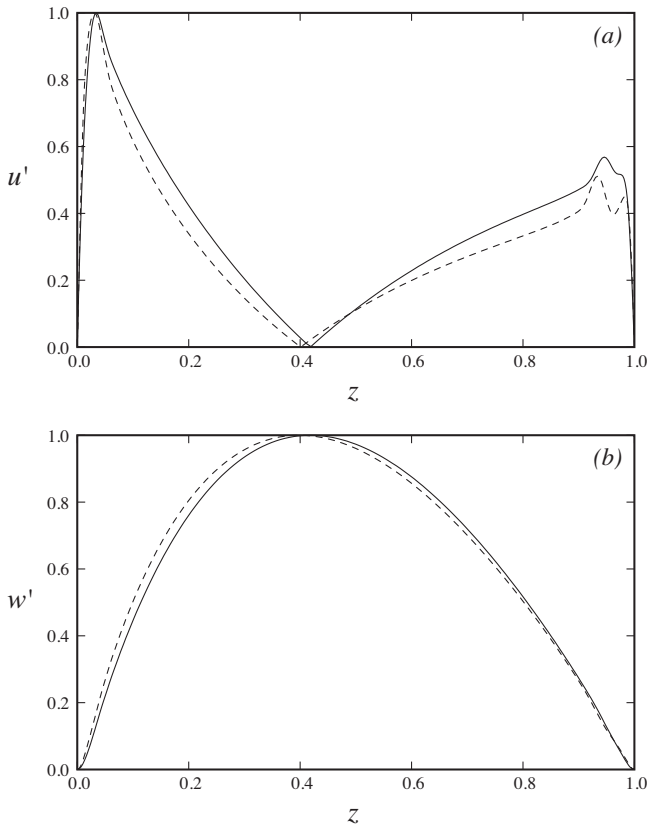

Fig. 6. Amplitudes of the normalised eigenfunctions u', plotted in panel (a), and w', plotted in panel (b). Dashed lines represent eigenfunctions on the upper branch and solid lines represent eigenfunctions on the lower branch.

onset instability occurs on the upper branch at $\theta = 0.0355^\circ$. The growth rates on both branches increase as the slope angle increases, and the growth rate on the upper branch is persistently higher than the lower branch.

Fig. 6 shows the amplitudes of the normalised eigenfunctions, namely u' and w', on the upper and lower branches. In plotting the eigenfunctions, the term $e^{i(\alpha x-\omega t)}$ is dropped out in the analysis and only the magnitude of u' and w', i.e. $\hat{u}$ and $\hat{w}$, are computed and shown. It is observed from Fig. 6(a) that the amplitude of the eigenfunction u' on the lower branch is larger than that on the upper branch, especially towards the upper edge of the downflow ($z = 1$). From Fig. 6(b), the eigenfunction w' on the lower branch also tend to skew towards the upper edge of the downflow. The eigenfunctions indicate that the two branches of instability have discernibly different most unstable disturbances and the slope angle has influences on the structure of ensuing instability.

5. Discussions

As reported previously, in the laboratory downflows on high slope angles have distinct characteristics that distinguish them from those on low slope angles. Specifically, for downflows on high slope angles, the scale of instability is larger in terms of amplitude and wavelength and the instability tends to skew towards the upper edge of the downflow. Moreover, field observations also indicate that a transition of flow may exist when the slope angle undergoes a small but abrupt decrease from 0.05° to 0.01°. Whether the flow transition as reported by Talling et al. (2007) is from one turbulent state to another or a reverse-transition process from turbulent to laminar flows is obscure, but for a geological flow on such a scale being laminar seems not very likely. Although our mathematical model of downflows may not exactly represent the conditions in the experiments and in the field observations as they are quite complex, it sheds some light on the underlying reason for downflows on high and low slope angles having distinct characteristics. With the idealised model, we observed that two branches of instability can occur for a downflow: the ensuing instability is on the lower branch for downflows on high slope angles and is on the upper branch for those on low slope angles. The amplitude and wavelength for the ensuing instability on the lower branch for high slope angles are both larger than those on the upper branch for low slope angles and the ensuing instability on high slope angles tends to skew towards the upper edge of the downflow. Our model also indicates that there exists a transitional slope angle, $\theta_E \approx 0.04^\circ$, across which the ensuing instability can switch from one branch to the other. Fortuitously, these findings resonate with and provide a theoretical support for previously reported observations.

Mindful that in the field the Reynolds number is likely in excess of $O(10^3)$. The nature of flow transition at such a high Reynolds number is inherently nonlinear. However, we do not intend to address the path of flow transition at such a high Reynolds number in this study but to provide one plausible heuristic explanation for the existence of two branches of instability, which are both supported by the gravity current down a slope.

Turbidity currents in the field are extremely difficult to monitor directly and analysis of such flows requires insightful and heuristic treatment. In the analysis, we adopted the Boussinesq approximation, which is essentially assuming that the density contrast caused by the suspended sediment particles is not very large so the non-Boussinesq effect can be neglected. Unlike flows driven by particles in the air, turbidity currents even with high sediment concentrations in a high-density carrier fluid such as water here may still be considered in the Boussinesq regime (Jacobson and Testik, 2013).

In addition the Boussinesq approximation, the heuristic model used in this study adopted other simplified elements such as flat top and bottom walls and linear density excess profile. In the field, neither the bottom is flat nor the top wall is present. Furthermore, the bottom in the field may exchange sediments with passing turbidity currents. The presence of the top wall inhibits the entrainment of ambient water and annihilates the long-term streamwise development of the thickness of gravity currents. Nevertheless, the heuristic model preserves a key element in the problem that the flow is purely driven by buoyancy while at the same time allows for a steady state solution based on which the stability analysis can be performed. As far as the stability properties are concerned, the streamwise development of the current can be ignored (Shringarpure et al., 2012). Regarding the density excess profile, the concentration profile depends on the properties of the sediment particles. From previous laboratory studies, several concentration profiles can exist but a linear profile is not unlikely in the experiments. Since turbidity currents are difficult to monitor in the field, we do not have the in situ concentration profile for the analysis but still we may choose one representative profile to illustrate the idea of two branches of instability in the flow. However, the model does not preclude other possibilities. There might be many complexities, such as the size of sediment particles, in the field and processes at work which may modify the density structures. These many complexities in the field are not likely to be incorporated into a theoretical model as designed here, however, from a perspective of flow stability, our heuristic model has demonstrated the existence of two branches of instability for a linearly stratified downflow. It should be pointed out that in our heuristic model, the particles do not settle out from the flow, or equivalently, the particle fall velocity is assumed zero. Strictly speaking, the analysis and the results presented in this study are perhaps more directly applicable to compositional gravity currents.

The slope angle comes into the problem mathematically only via the body force term in the wall-normal component of the momentum Eq. (10). The coefficient $1/\tan\theta$ in (10) can otherwise be identified as a 'bulk' Richardson number, *Ri*, which represents the ratio of potential energy due to stratification effect to kinetic energy of the flow. In the problem under investigation, the potential energy due to stratification effect scales as $\Delta\tilde{\rho}_b g\cos\theta\tilde{H}/\tilde{\rho}_0$, while the kinetic energy of the current scales as $\Delta\tilde{\rho}_b g\sin\theta\tilde{H}/\tilde{\rho}_0$. Therefore, the Richardson number is $Ri\sim 1/\tan\theta$, which suggests that the Richardson number decreases as the slope angle increases. As $\theta\to 90^\circ$, the stratification effect becomes unimportant in the flow, while as $\theta\to 0^\circ$, the stratification effect is dominant. In the problem under investigation, the flow is purely driven by the density excess and the Richardson number is simply related to the bed slope. As the slope angle decreases from 90° towards 0°, it is observed from Fig. 4 that the critical Reynolds number is relatively insensitive to the change in slope angle in the range of $10^\circ \lesssim \theta \leq 89^\circ$. For $\theta < 10^\circ$, the critical Reynolds number is more sensitive to the change in slope angle and increases rapidly when the slope angle further decreases.

It is intuitively understandable that the driving force for downflows diminishes as the slope angle decreases. Nevertheless, the role of Richardson number, played by the slope angle, θ, is less obvious. The stratification effect due to wall normal component of gravity increases as the slope angle decreases, therefore, the critical Reynolds number at the onset of instability increases as the slope angle decreases, as shown in Fig. 4. When a downflow propagates onto a sufficiently low slope angle during the course of its motion, as is the case of the continental slope on the ocean floor, the low driving force and intensified stratification effect would make the downflow less prone to sustain a turbulent state of flow, which ultimately leads to the final stage of a gravity current event.

Acknowledgements

The research is funded in part by Taiwan Ministry of Science and Technology through grant NSC-101-2628-E-002-039-MY3, 'Aim for Top University Project' of National Taiwan University through grant 103R7793, and TSUNG Cho-chang Education Foundation through grant 104-S-A10.

References

Adduce, C., Sciortino, G., Proietti, S., 2012. Gravity currents produced by lock-exchanges: experiments and simulations with a two layer shallow-water model with entrainment. J. Hydraul. Eng. 138 (2), 111–121.
Allen, J., 1985. Principles of Physical Sedimentology. Allen & Unwin.
Baines, P.G., 2001. Mixing in flows down gentle slopes into stratified environments. J. Fluid Mech. 443, 237–270.
Baines, P.G., 2005. Mixing regimes for the flow of dense fluid down slopes into stratified environments. J. Fluid Mech. 538, 245–267.
Beghin, P., Hopfinger, E.J., Britter, R.E., 1981. Gravitational convection from instantaneous sources on inclined boundaries. J. Fluid Mech. 107, 407–422.
Birikh, R.V., 1966. On small perturbations of a plane parallel flow with cubic velocity profile. Appl. Math. Mech. 30, 432–438.
Birikh, R.V., Gershuni, G.Z., Zhukhovitskii, E.M., Rudakov, R.N., 1968. Hydrodynamic and thermal instability of a steady convective flow. Appl. Math. Mech. 32, 246–252.

Birikh, R.V., Gershuni, G.Z., Zhukhovitskii, E.M., Rudakov, R.N., 1972. On oscillatory instability of plane-parallel convective motion in a vertical channel. Appl. Math. Mech 36, 707–710.
Bonometti, T., Balachandar, S., 2008. Effect of Schmidt number on the structure and propagation of density currents. Theor. Comp. Fluid Dyn. 22, 341–361.
Boyd, J.P., 2001. Chebyshev and Fourier Spectral Methods, 2nd ed. Dover.
Britter, R.E., Linden, P.F., 1980. The motion of the front of a gravity current travelling down an incline. J. Fluid Mech. 99, 531–543.
Cantero, M., Balachandar, S., Cantelli, A., Pirmez, C., Parker, G., 2009. Turbidity current with a roof: direct numerical simulation of self-stratified turbulent channel flow driven by suspended sediment. J. Geophys. Res. 114, C03008.
Cantero, M., Balachandar, S., Parker, G., 2009 January. Direct numerical simulation of stratification effects in a sediment-laden turbulent channel flow. J. Turbul. 10, 1–28.
Cantero, M., Lee, J., Balachandar, S., Garcia, M., 2007. On the front velocity of gravity currents. J. Fluid Mech. 586, 1–39.
Chandrasekhar, S., 1981. Hydrodynamic and Hydromagnetic Stability. Dover.
Chen, Y.M., Pearlstein, A.J., 1989. Stability of free-convection flows of variable-viscosity fluids in vertical and inclined slots. J. Fluid Mech. 198, 513–541.
Choux, C.M.A., Bass, J.H., McCaffrey, W.D., Haughton, P.D.W., 2005. Comparison of spatio-temporal evolution of experimental particulate gravity flows at two different initial concentrations, based on velocity, grain size and density data. Sedimentary Geology 179, 49–69.
Dai, A., 2010. Note on the generalized thermal theory for gravity currents in the deceleration phase. Dyn. Atmos. Oceans 50, 424–431.
Dai, A., 2013a. Experiments on gravity currents propagating on different bottom slopes. J. Fluid Mech. 731, 117–141.
Dai, A., 2013b. Power-law for gravity currents on slopes in the deceleration phase. Dyn. Atmos. Oceans 63, 94–102.
Dai, A., Garcia, M., 2010. Gravity currents down a slope in deceleration phase. Dyn. Atmos. Oceans 49, 75–82.
Drazin, P.G., Reid, W.H., 1981. Hydrodynamic Stability. Cambridge University Press.
Fannelop, T.K., 1994. Fluid Mechanics for Industrial Safety and Environmental Protection. Elsevier.
Felix, M., Sturton, S., Peakall, J., 2005. Combined measurements of velocity and cencentration in experimental turbidity currents. Sediment. Geol. 179, 31–47.
Hart, J.E., 1971. Stability of the flow in a differently heated inclined box. J. Fluid Mech. 47, 547–576.
Härtel, C., Meiburg, E., Necker, F., 2000. Analysis and direct numerical simulation of the flow at a gravity-current head. Part 1. Flow topology and front speed for slip and no-slip boundaries. J. Fluid Mech. 418, 189–212.
Hopfinger, E.J., 1983. Snow avalanche motion and related phenomena. Annu. Rev. Fluid Mech. 15, 47–76.
Huppert, H., 2006. Gravity currents: a personal perspective. J. Fluid Mech. 554, 299–322.
Jacobson, M.R., Testik, F.Y., 2013. On the concentration structure of high-concentration constant-volume fluid mud gravity currents. Phys. Fluids 25, 016602.
La Rocca, M., Adduce, C., Sciortino, G., Pinzon, A.B., 2008. Experimental and numerical simulation of three-dimensional gravity currents on smooth and rough bottom. Phys. Fluids 20 (10), 106603.
Marino, B., Thomas, L., Linden, P., 2005. The front condition for gravity currents. J. Fluid Mech. 536, 49–78.
Maxworthy, T., 2010. Experiments on gravity currents propagating down slopes. Part 2. The evolution of a fixed volume of fluid released from closed locks into a long, open channel. J. Fluid Mech. 647, 27–51.
McCaffrey, W.D., Choux, C.M., Bass, J.H., Haughton, P.D.W., 2003. Spatio-temporal evolution of velocity structure, concentration and grain-size stratification whithin experimental particulate gravity currents. Mar. Pet. Geol. 20, 851–860.
Necker, F., Härtel, C., Kleiser, L., Meiburg, E., 2005. Mixing and dissipation in particle-driven gravity currents. J. Fluid Mech. 545, 339–372.
Nielsen, M.H., Pratt, L., Helfrich, K., 2004. Mixing and entrainment in hydraulically driven stratified sill flows. J. Fluid Mech. 515, 415–443.
Rastello, M., Hopfinger, E.J., 2004. Sediment-entraining suspension clouds: a model of powder-snow avalanches. J. Fluid Mech. 509, 181–206.
Shin, J., Dalziel, S., Linden, P., 2004. Gravity currents produced by lock exchange. J. Fluid Mech. 521, 1–34.
Shringarpure, M., Cantero, M.I., Balachandar, S., 2012. Dynamics of complete turbulence suppression in turbidity currents driven by monodisperse suspensions of sediment. J. Fluid Mech. 712, 384–417.
Simpson, J., 1997. Gravity Currents, 2nd ed. Cambridge University Press.
Talling, P.J., Wynn, R.B., Masson, D.G., Frenz, M., Cronin, B.T., Schiebel, R., Akhmetzhanov, A.M., Dallmeier-Tiessen, S., Benetti, S., Weaver, P.P.E., Georgiopoulou, A., Zuhlsdorff, C., Amy, L.A., 2007. Onset of submarine debris flow deposition far from original giant landslide. Nature 450, 541–544.